

Effective Date:
Revision-

GSFC JPSS CMO
October 10, 2011
Released

**Joint Polar Satellite System (JPSS) Ground Project
Code 474
474-00043**

**Joint Polar Satellite System (JPSS)
Advanced Technology Microwave
Sounder (ATMS)
SDR Radiometric Calibration
Algorithm Theoretical Basic
Document (ATBD)**

For Public Release

The information provided herein does not contain technical data as defined in the International Traffic in Arms Regulations (ITAR) 22 CFC 120.10. This document has been approved For Public Release to the NOAA Comprehensive Large Array-data Stewardship System (CLASS).



National Aeronautics and
Space Administration

**Goddard Space Flight Center
Greenbelt, Maryland**

This page intentionally left blank.

**Joint Polar Satellite System (JPSS) (JPSS)
Advanced Technology Microwave Sounder (ATMS)
SDR Radiometric Calibration
Algorithm Theoretical Basic Document (ATBD)**

JPSS Electronic Signature Page

Reviewed By:

Neal Baker
JPSS Data Products and Algorithms, Senior Engineering Advisor
(Electronic Approvals available online at https://jpssmis.gsfc.nasa.gov/mainmenu_dsp.cfm)

Approved By:

Heather Kilcoyne
DPA Manager
(Electronic Approvals available online at https://jpssmis.gsfc.nasa.gov/mainmenu_dsp.cfm)

**Goddard Space Flight Center
Greenbelt, Maryland**

This page intentionally left blank.

Preface

This document is under JPSS Ground Algorithm ERB configuration control. Once this document is approved, JPSS approved changes are handled in accordance with Class I and Class II change control requirements as described in the JPSS Configuration Management Procedures, and changes to this document shall be made by complete revision.

Any questions should be addressed to:

JPSS Ground Project Configuration Management Office
NASA/GSFC
Code 474
Greenbelt, MD 20771

This page intentionally left blank.

Change History Log

Revision	Effective Date	Description of Changes (Reference the CCR & CCB/ERB Approve Date)
Original	04/22/2011	474-CCR-11-0058: This version baselines D43751, Rev C dated 03/12/2007. This is the version that was approved for NPP launch. Per NPOESS CDFCB - External, Volume V – Metadata, doc number D34862-05, this has been approved for Public Release into CLASS. This was approved at the JPSS Ground Algorithm ERB April 22, 2011.

This page intentionally left blank.

Northrop Grumman Space & Mission Systems Corp.
Space Technology
One Space Park
Redondo Beach, CA 90278

NORTHROP GRUMMAN

Raytheon



Engineering & Manufacturing Development (EMD) Phase
Acquisitions & Operations Contract

CAGE NO. 11982

**Advanced Technology Microwave Sounder (ATMS)
SDR Radiometric Calibration
Algorithm Theoretical Basic Document (ATBD)**

DATE: 12 March 2007

**No. D43751
REV. C**

PREPARED BY: _____
Ronson Chu, Models & Simulations

ELECTRONIC APPROVAL SIGNATURES:

Merit Shoucri, Models & Simulation Lead

Prepared by
Northrop Grumman Space Technology
One Space Park
Redondo Beach, CA 90278

Prepared for
Department of the Air Force
NPOESS Integrated Program Office
C/O SMC/CIK
2420 Vela Way, Suite 1467-A8
Los Angeles AFB, CA 90245-4659

Under
Contract No. F04701-02-C-0502

COMMERCE DESTINATION CONTROL STATEMENT

The export of these commodities, technology or software are subject to the U.S. Export Laws and Regulations in accordance with the Export Administration Regulations. Diversion contrary to U.S. law is prohibited.



Northrop Grumman Space & Mission Systems Corp. Space Technology One Space Park Redondo Beach, CA 90278		 	
Revision/Change Record		For Document No. D43751	
Revision	Document Date	Revision/Change Description	Pages Affected
---	02 Feb 2007	Initial PCIM Release to bring document into Matrix Accountability. Reference NASA original document delivered in 2005	All
A	8 Feb 2007	The ATBD has been modified under SPCR 1114. The science codes have been modified under SPCR 1071.	9,11,13, 16,23-27
B	12 March 2007	Reference ECR-A116. This release of the ATMS SDR Radiometric Calibration ATBD is associated with the post drop release of science algorithm update, test data, test result and documentation (ISTN_ATMS_NGST_3.1), The ATBD has been modified under SPCR 1146. The science codes have been modified under SPCR 1145.	7,26
C	27 Jan 2010	In preparation for Public Release of this ATBD, the following administrative changes were made: all ITAR markings were removed, and Distribution Statement F added.	All

Table of Contents

Acronyms	v
1 Introduction	1
2 Historical Perspective	3
3 Instrument Description	5
4 Instrument Interoperability	10
5 In-flight Calibration System	11
5.1 Blackbody view	13
5.2 Cold space view	14
5.3 Sources of errors and uncertainties	17
6 Calibration Processing Steps	21
6.1 Physical temperatures	21
6.2 Effective blackbody brightness temperature	22
6.3 Effective space brightness temperature	23
6.4 Radiometric calibration counts	24
6.5 Earth scene brightness temperatures	25
6.6 Data quality control	25
7 Scan Bias Correction	27

Illustrations

Figure 1	NPP spacecraft	1
Figure 2	ATMS instrument layout	5
Figure 3	ATMS antenna and RF feed subsystem	5
Figure 4	Typical microwave antenna pattern	6
Figure 5	ATMS block diagram	6
Figure 6	Polarization vectors	8
Figure 7	Scan sequence	9
Figure 8	Transfer function	11
Figure 9	Typical warm load	13
Figure 10	Space view geometry	15
Figure 11	Calibration flow chart	21

Tables

Table 1	ATMS spectrometric and radiometric specifications	8
---------	---	---

Acronyms

ADC	Analog-to-digital converter
AIRS	Atmospheric Infrared Sounder
AMSU	Advanced Microwave Sounding Unit
ARM	Atmospheric Radiation Measurement program
ATBD	Algorithm Theoretical Basis Document
ATMS	Advanced Technology Microwave Sounder
ATOVS	Advanced TOVS
CDR	Climate Data Record
CrIMSS	Cross-track Infrared and Microwave Sounding Suite
CrIS	Cross-track Infrared Sounder
DN	Data number
EDR	Environmental Data Record
EDU	Engineering Development Unit
EOS	Earth Observing System
EOSDIS	EOS Data and Information System
EU	Engineering unit
FRD	Functional Requirements Document
GSFC	Goddard Space Flight Center
HAMSR	High Altitude MMIC Sounding Radiometer
HIRS	High resolution Infrared Radiation Sounder
IF	Intermediate frequency
IMAS	Integrated Multispectral Atmospheric Sounder
IPO	Integrated Program Office
IORD	Integrated Operational Requirements Document
IR	Infrared
JPL	Jet Propulsion Laboratory
LO	Local oscillator
MHS	Microwave Humidity Sounder
MIT	Massachusetts Institute of Technology
MMIC	Monolithic Microwave Integrated Circuit
MSU	Microwave Sounding Unit
MUX	Multiplexer
MW	Microwave
NASA	National Aeronautic and Space Administration
NEDT	Noise-equivalent delta-T
NGES	Northrop Grumman Electronic Systems
NGST	Northrop Grumman Space Technologies
NOAA	National Oceanic and Atmospheric Administration
NPOESS	National Polar-orbiting Operational Environmental Satellite System
NPP	NPOESS Preparatory Project
NWP	Numerical Weather Prediction
NWS	National Weather Service
ORD	Operational Requirements Document
PLLO	Phase locked local oscillator
POES	Polar-orbiting Operational Environmental Satellite

POS	P erformance and O perations S pecification
PRT	P latinum r esistance t hermometer
QA	Q uality a ssessment
QC	Q uality c ontrol
RDR	R aw D ata R ecord
RF	R adio f requency
SDR	S ensor D ata R ecord
SSM/IS	S pecial S ensor — M icrowave I mager/ S ounder
SSM/T	S pecial S ensor — M icrowave T emperature s ounder
TIROS	T ele v ision I nfrared O bservation S atellite
TOVS	T IROS O perational V ertical S ounder
WMO	W orld M eteorological O rganization

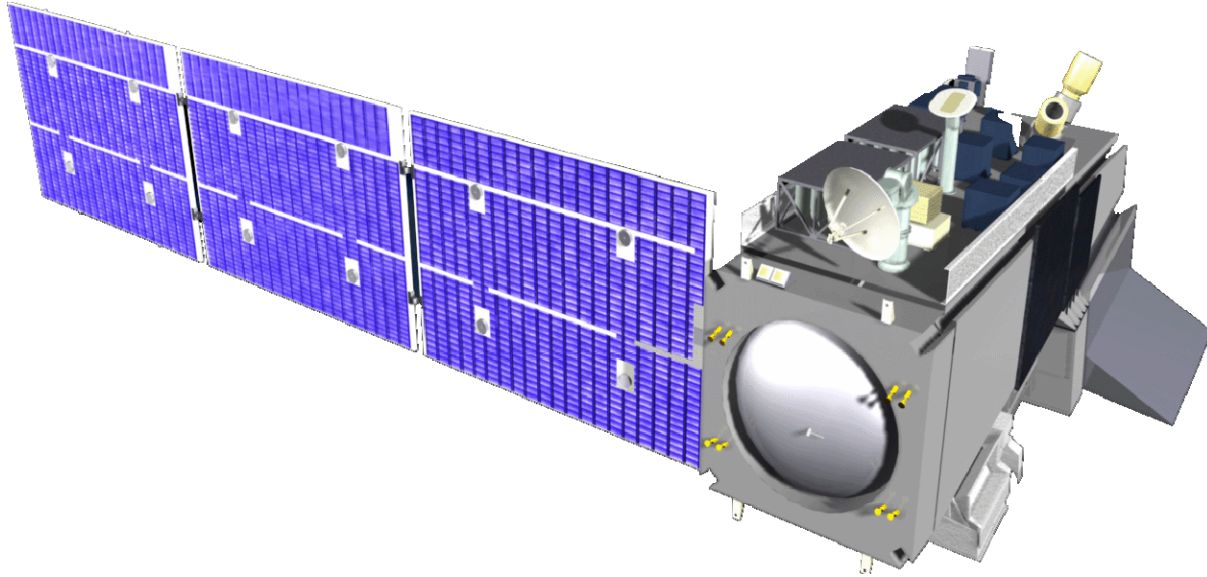


Figure 1: NPP spacecraft

1 Introduction

This Algorithm Theoretical Basis Document (ATBD) describes the theoretical basis and, to a limited extent, the implementation of the algorithms used to convert raw data numbers (DN) or engineering units (EU) from the telemetry of the ATMS instrument, contained in the Raw Data Records (RDR) to calibrated brightness temperatures, contained in the Sensor Data Records (SDR). The RDRs (i.e. raw and minimally processed telemetry) make up the input to the SDR process, while the latter — the output from the SDR process — make up the input to the Environmental Data Record (EDR) process, where the calibrated radiances from CrIS and calibrated brightness temperatures from ATMS are converted to geophysical parameters through a “retrieval” process.

Two major elements of the proposed SDR processing are not discussed here: geolocation and spatial resampling, since those elements do not affect the radiometric calibration (although they may affect errors and uncertainties).

The algorithms described in this document are very similar to those that have been developed by NOAA and NASA for the AMSU-A and -B instruments, which have flown since 1998 (NOAA) and 2002 (NASA), respectively. Details of the description are based on preliminary software developed by the ATMS contractor, NGES, and delivered in mid-2004 as version 2.2. The initial version of this document was revised to include algorithm changes that NGST implemented. It is expected that this document will be updated to reflect major revisions of the SDR code as there are changes in the theoretical basis or the formulation of the underlying algorithms. Since the basic functionalities and principles of operation of these instruments are quite similar, the

differences between the respective algorithmic approaches are relatively minor. For example, while NOAA prefers to convert radiometer measurements to physical radiance units ($\text{mW}/\text{m}^2\text{-sr}\text{-cm}^{-1}$), the approach of NASA is to convert to brightness temperature units (K) instead, which is the most common practice in the microwave field. It is a simple matter to convert between the two.

It is the intention that this ATBD be readable as a standalone document, although *it is recommended that the reader reference related instrument and system description documents available from NGES, NGST, IPO and NASA*. In what follows there is a brief description of the instrument itself, in order to explain references to devices, procedures and tables used by the SDR algorithms. However, for a full understanding of the hardware and the measurement system, the reader should also refer to the CrIS SDR ATBD, the CrIMSS EDR ATBD, and the respective requirements documents (ORDs and POSs) and relevant hardware and software description documents. The present document reflects as-built performance characteristics to the extent they are known, and otherwise assumes full compliance of the hardware with the specifications.

This document describes the *functions* performed by the ground data system. However, it should be noted that nothing should be implied about the *architecture* or the *implementation* of the system. Thus, algorithms that may be described here as if they were to be executed in conjunction with each other could in fact be executed in isolation from each other. For example, data quality checking belonging to individual steps may be consolidated and executed before those step are reached in the actual processing system, in order to provide an efficient implementation. Also, in some instances there may be essential elements missing from the software implementation – those will be noted in the text and in a companion commentary.

Acknowledgments

Much of the illustrative material in this document has been “borrowed” from material provided by NGES. Also, the ATMS SDR Algorithm Description¹ document accompanying the SDR v.2.2 code delivery has been very helpful in putting the present document together.

¹ K. Anderson: “ATMS SDR Algorithm Description”; NGES TM-01-380D (2004)

2 Historical perspective

The Advanced Technology Microwave Sounder (ATMS), together with the Crosstrack Infrared Sounder (CrIS) — a high spectral resolution IR spectrometer — are designed to meet the measurement requirements set for the National Polar-orbiting Operational Environmental Satellite System (NPOESS) as well as satisfy the climate research objectives of the National Aeronautics and Space Administration (NASA). The first version of this Crosstrack Infrared Microwave Sounding Suite (CrIMSS) will be operated by the Integrated Program Office (IPO) on the NPOESS Preparatory Project (NPP) mission and subsequently on a series of NPOESS missions. NPP serves the two functions of providing risk reduction for NPOESS and providing science data continuity between the NASA Terra and Aqua missions (the latter being the first mission to carry a high resolution sounding suite) on one hand and NPOESS on the other. For that reason, the NPP mission has sometimes been called the “bridging mission”. Additionally, while NPOESS is primarily designed to support operational weather forecasting needs, NASA has a strong interest in research and climate applications, and an effort is under way to determine how NPOESS can satisfy those needs. Thus, the third function of NPP is to serve as a testbed for transforming weather satellite data to climate research quality data.

The High Resolution Infrared Sounder (HIRS) and the Microwave Sounding Unit (MSU), together forming the TIROS Operational Vertical Sounder (TOVS) on the NOAA polar orbiting environmental satellite system (POES), have supported the National Weather Service (NWS) forecasting effort with global temperature and moisture soundings since the late 70's. In the course of the years HIRS has been periodically upgraded, and in 1998 a jump was made from MSU to the Advanced Microwave Sounding Unit (AMSU). The combined HIRS/AMSU system is called the Advanced TOVS (ATOVS) and now forms the backbone of the NOAA POES systems. It is expected to operate until NPOESS comes on line.

During the mid-1980's, while TOVS was still flying, it was determined that future numerical weather prediction (NWP) data needs would soon require satellite sounders with accuracies equivalent to radiosondes. An effort was launched by NASA to develop the technology and capability to achieve that. The result was the Atmospheric Infrared Sounder (AIRS), which, together with an AMSU microwave suite, was launched as part of the Aqua mission in 2002. AIRS is the first of a coming series of high spectral resolution IR sounders, and it has already demonstrated the utility of radiosonde quality satellite soundings – AIRS data is now being assimilated by a number of NWP centers, largely still on an experimental basis, and is having significant positive forecast impact. While CrIS uses a different measurement approach (it is a Fourier transform spectrometer, while AIRS is a grating spectrometer), it is the successor of AIRS and is expected to have comparable performance. Other instruments in the same class are being developed elsewhere.

During the mid-1990's, while AIRS was being built, an effort was made by NASA to transfer the AIRS technology to the IPO, with the goal of providing an AIRS follow-on for the NPOESS missions. Again, a technology development effort was launched – this time primarily focused on reducing the mass, size and power consumption of the microwave component of the sounding suite. The proposed system was called the Integrated Multispectral Atmospheric Sounder (IMAS) – a single combined infrared and microwave instrument that was intended to fly as a demonstration on the NASA New Millennium Program's EO-3 mission. The effort was

terminated in mid-1998 largely due to cost constraints, but many of the IMAS microwave specifications were later adopted for the ATMS instrument.

It was initially the intention to use the 118-GHz oxygen line for temperature sounding in the IMAS system, instead of the 50-60 GHz band used by AMSU. This would make it possible to shrink the aperture by a factor of more than 2 (and therefore also the overall mass and size) while maintaining spatial resolution and other performance measures. A field of view (FOV) of the same size as the IR sounder (i.e. 1.1°) was highly desired, and the IMAS/MW component was therefore designed to have that beam width for all sounding channels (i.e. in the 118-GHz band for temperature sounding and in the 183-GHz band for water vapor sounding). Later, it was realized that even the most transparent 118-GHz channels may not be able to penetrate to the surface under very humid and cloudy conditions (e.g., in the tropics), and the 50-GHz band was restored to provide backup capabilities for such situations. A compromise was made to use the same aperture size at 50 GHz as at 118 GHz, and a 2.5° beam width resulted. The IMAS team also determined that the microwave instrument should have the same spectral channels as AMSU for “science continuity” and that a few additional channels were desirable. Thus, two channels were added in the 183-GHz band, and one window channel was added in the 50-GHz band. In addition, the 150-GHz quasi-window channel used in AMSU-B was replaced with one at 166 GHz, which can be operated as part of an advanced-technology 183-GHz receiver (thus saving one receiver chain). This concept had been developed earlier by the AIRS team. Most of these specifications and characteristics are now part of the ATMS specifications, but the 118-GHz band was eliminated early in the program due to cost constraints, and 2.5° was improved to 2.2° .

The most significant advance under IMAS was the development of monolithic microwave integrated circuit (MMIC) technology at sounding frequencies (i.e. at 50, 118 and 183 GHz) – previously only available at considerably lower frequencies, which would allow for sensitive and compact receivers and spectrometers. Sample receivers were developed for the two lower bands, and low noise amplifiers (i.e. precursors to full receivers) were developed for the 183-GHz band, and compact solid-state filter banks were developed for the two lower bands. After the termination of IMAS these technology items were incorporated into an aircraft based microwave sounder, the High Altitude MMIC Sounding Radiometer (HAMSR), developed under the NASA Instrument Incubator Program. HAMSR may be viewed as an ATMS precursor and prototype in many respects (e.g., HAMSR uses a dual aperture, with two reflectors operating on a common axis, just as was later adopted for ATMS). HAMSR has been successfully operated on the NASA ER-2 high altitude aircraft since 2001. In summary, ATMS has heritage primarily from AMSU and from the IMAS design (and its HAMSR spin-off).

3 Instrument Description

In this section we give a brief description of the ATMS instrument, illustrated in Fig. 2. ATMS is

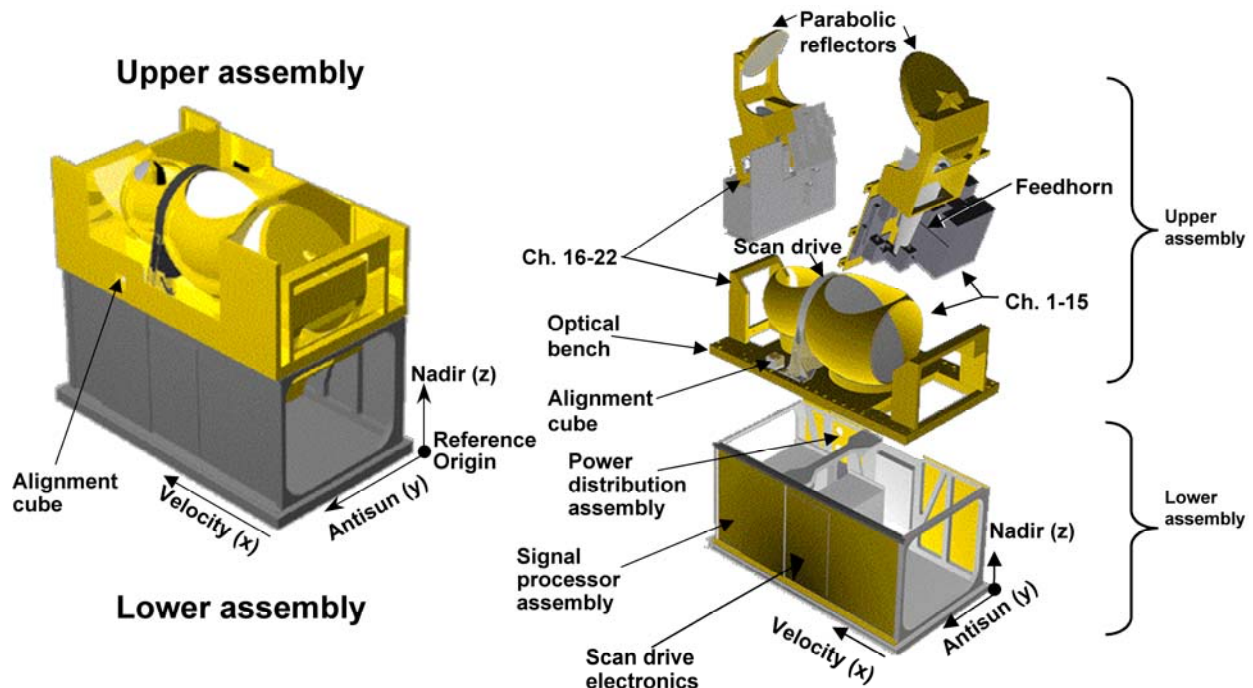


Figure 2: ATMS instrument layout

a 22-channel microwave sounder providing both temperature soundings – between the surface and the upper stratosphere (i.e. to about 1 mb, at an altitude of about 45 km) – and humidity soundings – between the surface and the upper troposphere (i.e. to about 200 mb, at an altitude of about 15 km). Like AMSU, it is a crosstrack scanner. There are two receiving antennas — one serving 15 channels below 60 GHz (with a beam width of 2.2° for all except the lowest two channels) and one serving 7 channels above 60 GHz (with a beam width of 1.1° for all except the lowest channel). The antennas consist of plane reflectors mounted on a scan axis at a 45° tilt angle, so that radiation is reflected from a direction perpendicular to the scan axis into a direction along the scan axis (i.e. a 90° reflection). With the scan axis oriented in the along-track direction, this results in a cross-track scan pattern. The reflected radiation is in each case focused by a stationary parabolic reflector onto a dichroic plate and from there either reflected to or passed through to a feedhorn. Each aperture/reflector therefore serves two frequency bands, for a total of four bands. Thus, radiation from a direction within the scan plane, which depends on the angle of rotation of the reflector, is reflected and focused onto the receiver apertures — conical feedhorns. This is illustrated schematically in Fig. 3.

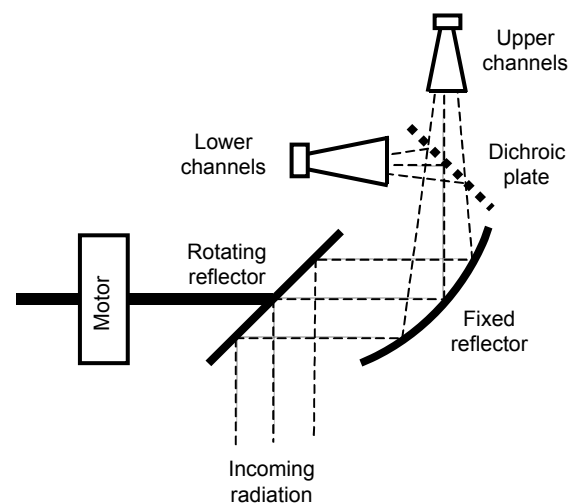


Figure 3: ATMS antenna and RF feed subsystem (schematically); one of two

The design of the antenna system is such that a slightly diverging conical pencil "beam" is formed which has a half-power width (also called the 3-dB width) of either 1.1°, 2.2° or 5.2°, with a possible ±10% variation from channel to channel. Each beam is approximately Gaussian-shaped at the center and receives a significant portion of its energy outside the half-power cone. Approximately 95-97% of the energy is received within the so-called main beam, which is defined as 2.5 times the half-power beam width — i.e. the ATMS "main beam" is either 2.75°, 5.5° or 13° wide. Significant energy (i.e. up to 5%) is thus received from outside the main beam. Fig. 4 shows a typical antenna pattern. The pattern in the vicinity of the main beam is called the near sidelobes, while that further away is called the far sidelobes. The far sidelobes contribute significantly to the measurement errors.

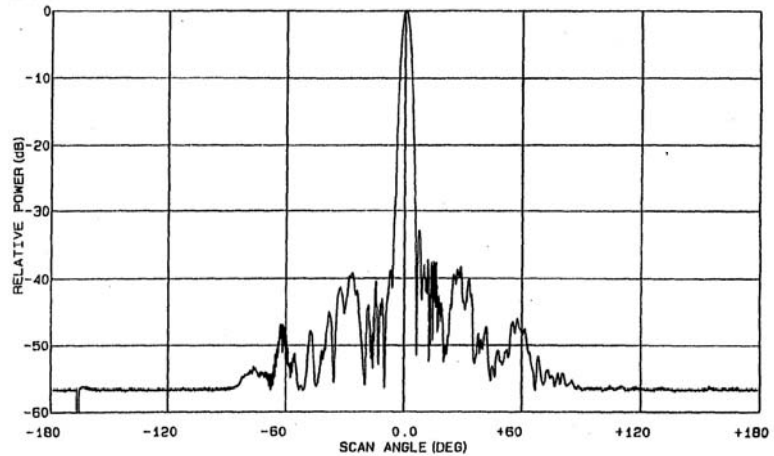


Figure 4: Typical microwave antenna pattern

The feedhorn is for some bands followed by a diplexer that splits the RF energy into two parallel signal paths that proceed to the respective receiver, which is in most cases a heterodyne system. There, each sub-band is down converted by a mixer, separated into channels with filters, and detected. Fig. 5 shows a block diagram of the ATMS system. In the following paragraphs we

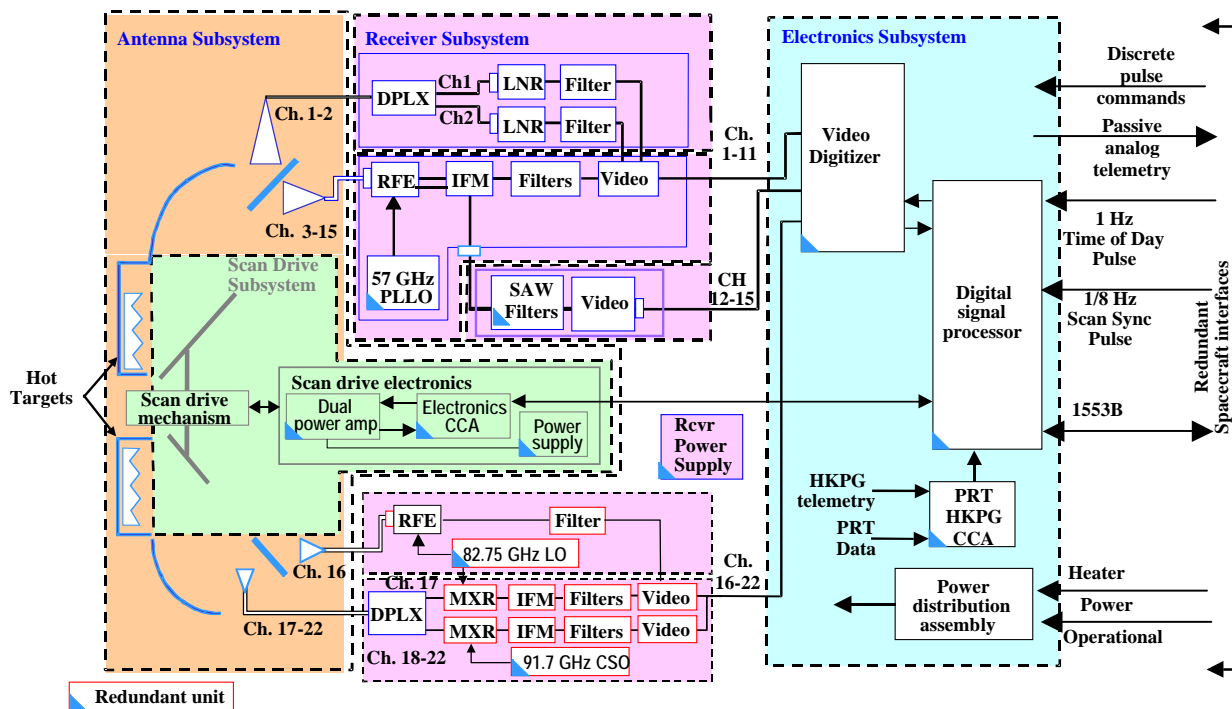


Figure 5. ATMS block diagram

will discuss the various signal paths that lead to the individual spectral channel outputs.

The larger of the two apertures is used for the 15 lowest-frequency channels and is sometimes referred to as the KAV-aperture, since it covers K-band (channel 1), Ka-band (channel 2) and V-band (channels 3-15). Here the dichroic plate, which reflects frequencies below a certain value and transmit those above, splits the RF energy into a low frequency path (reflected) and a high frequency path (transmitted). The output of the low frequency feedhorn enters a diplexer, which in turn splits the now somewhat band limited RF energy into two parallel paths. Each is fed into an amplified receiver chain followed by a bandpass filter – one centered at 23.8 GHz (channel 1) and one centered at 31.4 GHz (channel 2). These are the only non-heterodyne receivers in the ATMS system.

The output of the higher frequency feedhorn is fed into an amplified and bandpass filtered heterodyne receiver with two down-converter/mixer chains, both fed by a common local oscillator (LO) operating at 57.290344 GHz. (This is a highly stable and temperature controlled crystal referenced phase locked oscillator.) One path is low pass filtered, and the result is a single-sideband intermediate frequency (IF) band located at 1.6 – 7.1 GHz below the LO frequency. This band is in turn passed through a set of signal splitters/multiplexers and bandpass filters that select channels 3-9. The other path is bandpass filtered, and the result is a double-sideband IF band located 10 – 400 MHz away from the LO frequency. Two channels (10 and 11) are formed with conventional bandpass filters similar to those used for channels 3-9, while the rest (12-15) are formed with a standing acoustic wave (SAW) filter assembly. Note that the SAW assembly is implemented as a set of four pairs of filters, each positioned symmetrically with respect to an IF frequency of 322.2 MHz. The outputs of each filter pair are combined and amplified. Channels 12-15 are therefore in effect quadruple-sideband channels.

The smaller aperture is used for the 7 highest frequency channels and is sometimes referred to as the WG-aperture, since it covers W-band (channel 16) and G-band (channels 17-22). Here the lower frequency path (i.e. reflected from the dichroic plate) enters a single feedhorn and an amplified highpass filtered heterodyne receiver chain, where the mixer uses an LO operating at 82.75 GHz, producing a single upper sideband IF signal that is put through a 4450-6450 MHz bandpass filter for channel 16 (which results in a channel located at 87.2-89.2 GHz). The high frequency path (i.e. that transmitted through the dichroic plate) enters a smaller feedhorn followed by a diplexer that splits the signal into two paths. One path goes to a second harmonic mixer that uses the same LO as the channel 16 receiver. The resulting double sideband IF signal is put through a 350-1500 MHz bandpass filter for channel 17 (which is then located at 164-167 GHz with a gap at 165.15-165.85 GHz). The second path also goes to a second harmonic mixer, but it uses an LO operating at 91.655 GHz. The double sideband IF is passed through a set of filters that produce channels 18-22. (Those channels are therefore centered at $183.31 \text{ GHz} \pm \Delta f$, where Δf is 7, 4.5, 3, 1.8 or 1 GHz, and the bandpass width varies from channel to channel.)

Table 1 summarizes the performance specifications of all 22 channels, including radiometric sensitivity – usually called noise equivalent temperature change and denoted as NEDT. The table lists three frequency specifications: nominal center frequency, center frequency stability (i.e. the maximum deviation allowed from the nominal center frequency value), and specified and as-built bandwidth. All are given in MHz. The as-built bandwidth notation is "N \times Δf ", where N is the number of sub-bands used for a channel and Δf is the width of each sub-band. (E.g., 2 \times 270 means this is a double-band channel, with each of the two bands being 270 MHz wide.)

Beamwidth is also listed. Finally, the polarization of each channel is listed. A single linear polarization is measured for each channel, and Table 1 lists the nominal polarization direction at the nadir scan position.

Table 1. ATMS spectrometric and radiometric specifications

Ch	RF path			Center frequency [MHz]		Bandwidth [MHz]		NEDT [K]	Pol	Beamwidth
	Ant	Feed	Rcvr	Value	Stab	Req	True	Req		[°] Req
1	A	1	a	23800	<10	<270	1x270	0.5	V	5.2
2	A	1	b	31400	<10	<180	1x180	0.6	V	5.2
3	A	2	c	50300	<10	<180	1x180	0.7	H	2.2
4	A	2	c	51760	<5	<400	1x400	0.5	H	2.2
5	A	2	c	52800	<5	<400	1x400	0.5	H	2.2
6	A	2	c	53596±115	<5	170	2x170	0.5	H	2.2
7	A	2	c	54400	<5	400	1x400	0.5	H	2.2
8	A	2	c	54940	<10	400	1x400	0.5	H	2.2
9	A	2	c	55500	<10	330	1x330	0.5	H	2.2
10	A	2	d ₁	57290.344 [f ₀]	<0.5	330	2x155	0.75	H	2.2
11	A	2	d ₁	f ₀ ±217	<0.5	78	2x 78	1.0	H	2.2
12	A	2	d ₂	f ₀ ±322.2±48	<1.2	36	4x 36	1.0	H	2.2
13	A	2	d ₂	f ₀ ±322.±22	<1.6	16	4x 16	1.5	H	2.2
14	A	2	d ₂	f ₀ ±322.±10	<0.5	8	4x 8	2.2	H	2.2
15	A	2	d ₂	f ₀ ±322.±4.5	<0.5	3	4x 3	3.6	H	2.2
16	B	3	e	88200	<200	2000	1x2000	0.3	V	2.2
17	B	4	f	165500	<200	3000	2x1150	0.6	H	1.1
18	B	4	g	183310±7000	<30	2000	2x2000	0.8	H	1.1
19	B	4	g	183310±4500	<30	2000	2x2000	0.8	H	1.1
20	B	4	g	183310±3000	<30	1000	2x1000	0.8	H	1.1
21	B	4	g	183310±1800	<30	1000	2x1000	0.8	H	1.1
22	B	4	g	183310±1000	<30	500	2x 500	0.9	H	1.1

Because of the rotating main reflector, the detected polarization vector rotates as the scan reflector rotates. (This can be understood by envisioning the detected polarization vector, which is fixed relative to the feedhorn, being projected onto the ground below – by simple geometric imaging.) The direction indicated in Table 1 as “V” corresponds to a direction that lies in the scan plane, while “H” is the direction that is perpendicular to the scan plane – i.e. in the horizontal plane. (At nadir these two polarizations are of course degenerate, i.e. observed emissions would be identical for an isotropic surface.) As the scanner rotates the beam away from nadir, the detected “V” polarization also rotates out of the scan plane while the detected “H” polarization rotates out of the perpendicular plane and thus also out of the horizontal plane. The angle of rotation away from the respective planes equals the scan angle relative to nadir. This is illustrated schematically in Figure 6, which shows the projection of the various polarization vectors in the plane perpendicular to the ray path (i.e. the plane that contains the electromagnetic field vectors). This plane coincides with the horizontal plane for the nadir scan position but rotates as the scan position rotates. In addition, as explained above, the “H” and “V” polarization vectors rotate within this plane. When surface emissivity and similar quantities are computed, it is important to correctly transform between the observed “H” and “V” vectors and the local

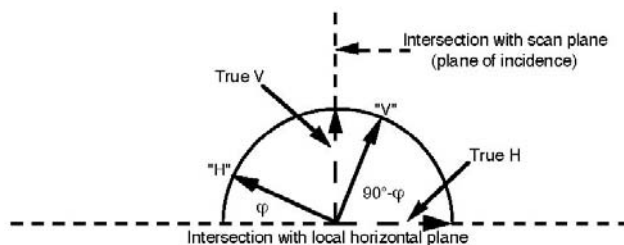


Figure 6. Polarization vectors, in the transverse

true H and V vectors as computed from models.

The antenna reflectors rotate continuously counter-clockwise relative to the spacecraft direction of motion (i.e. the spin vector points in the negative x-direction while the spacecraft moves along the positive x-direction), completing three revolutions in 8 seconds. The scan mechanism is synchronized to the spacecraft clock with a “sync” pulse every 8 seconds (i.e. for every third revolution). Each scan cycle is divided into three segments. In the first segment the earth is viewed at 96 different angles, symmetric around the nadir direction. The antenna is in continuous motion, and the 96 samples are taken “on the fly”, with each sample representing the mid-point of a brief sampling interval of about 18 ms. The scan speed is such that the corresponding angular sampling interval is 1.11° (i.e. the scan speed is about $61.6^\circ/\text{second}$). The angular range between the first and last sample centroids is therefore 105.45° (i.e. $\pm 52.725^\circ$ relative to nadir). The antenna then accelerates and moves to a position that points it toward an unobstructed view of space (i.e. between the earth's limb and the spacecraft horizon). There it resumes the same slow scan speed as maintained across the Earth scenes while four consecutive cold calibration measurements are taken. Next, the antenna is again accelerated to the zenith direction, which points it toward an internal calibration target that is at the relatively high ambient instrument temperature, and is again slowed down to normal scan speed while four consecutive warm calibration measurements are taken. Finally, it is accelerated to the starting Earth scene position, where it is slowed down to normal scan speed to begin another scan cycle. Every third cycle the synchronization signal arrives just before the start position is reached and is used to maintain this pattern through a phase locked loop. Fig. 7 illustrates this — the normal operational scan mode.

(There is also a stare mode, where the antenna can be pointed to the nadir direction or either of the calibration directions for an extended period of time, but that is only used for special purposes.) Each of the 96 earth samples takes about 18 milliseconds, for a total of approximately 1.73 seconds. The “duty cycle” of ATMS is therefore about 65%, i.e. about 65% of the scan cycle period is dedicated to Earth observations.

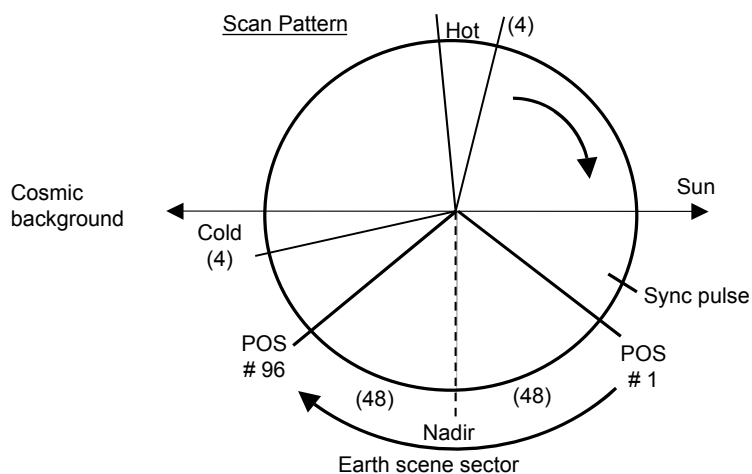


Figure 7. Scan sequence (flight direction is toward the reader)

4 Instrument Interoperability Issues

As described earlier, the CrIS/ATMS instrument suite forms a single sounding system (CrIMSS), even though it consists of two independent instrument modules, and the retrieval approach is based on the assumption that the two instruments are viewing the same air mass and surface “footprint” at the same time. This requires both alignment and synchronization. The details are beyond the scope of this document, and here we will simply point out that there are differences between the operational aspects of CrIS and ATMS that present challenges to achieving this goal. For example, CrIS completes a single scan cycle in 8 seconds, with 30 samples of a 3x3 cluster of individual FOVs and each cluster separated by 3.33° . While the resulting spatial sampling density is nearly identical to that of ATMS, their scan speeds differ markedly (i.e. three vs. one scan cycle every 8 seconds), which causes significant alongtrack misalignment at the scan swath edges. Alignment may be optimized (but not made perfect, due to the fact that the CrIS 3x3 sample cluster rotates with scan angle in a manner similar to that of the ATMS polarization vectors) by mounting CrIS with a slight (less than 1°) positive yaw angle relative to ATMS (or mount ATMS with a negative yaw relative to CrIS). Synchronization is more easily achieved, by introducing a time offset between the occurrence of the 8-second sync pulse and the start of a new scan cycle (which is defined as the start of the first Earth sample interval). ATMS has been designed to allow for such a delay, with a value that can be commanded from the ground. The objective of co-alignment and synchronization is usually to achieve close spatial coincidence between the respective “footprint” patterns projected on the ground. The AIRS-AMSU system incorporates both a yaw correction and synchronization, but the HIRS-AMSU system does not. Instead, NOAA data is spatially interpolated, to achieve a synthesized alignment. Since such an approach is vulnerable to processing artifacts, the preferred method is physical alignment and synchronization to the extent possible. The CrIS-ATMS system relies on a Backus-Gilbert algorithm to generate ATMS footprints that match the CrIS footprints both in size and location. A study² has shown that with the proper footprint matching algorithm, the difference between having mechanical alignment and without such alignment is small.

² William J. Blackwell and Frederick W. Chen: “SDR Impact of Known CrIMSS Yaw Rotation Offsets”, MIT Lincoln Laboratory (Nov. 20, 2005)

5 In-flight Calibration System

As described in Section 3 (Instrument description), and illustrated in Fig. 7 (scan sequence), each of the two ATMS antenna/receiver systems measures the radiation from two calibration sources during every scan cycle. The first source is the cosmic background radiation emanating from space. This source is viewed immediately after the earth has been scanned. The antenna is quickly moved to point in a direction between the earth's limb and the spacecraft's horizon. There it drifts slowly while 4 measurements are taken. The second source is an internal blackbody calibration target (often called a "warm load"), which is at the ambient internal instrument temperature. This source is viewed immediately after the space calibration view; the antenna is again quickly moved, to point in the zenith direction, where the blackbody target is located. Again, the antenna drifts slowly while 4 measurements are taken. Thus, two sets of calibration measurements that bracket the earth scene measurements are obtained for every scan cycle. A full discussion of calibration issues can be found in a document produced by NGES³.

Such a through-the-antenna calibration system allows most system losses and instrument defects to be calibrated, since the calibration measurements involve the same optical and electrical signal paths as earth scene measurements. (The only exception is that the internal calibration target appears in the antenna near field and can reflect leakage emission from the antenna itself. That effect is taken into account with so-called bias corrections in the calibration processing, however.) This approach has an advantage over calibration systems using switched internal noise sources injected into the signal path after the antenna, at the cost of some weight gain since the internal calibration target is fairly massive.

The purpose of the calibration measurements is to accurately determine the so-called radiometer transfer function, which relates the measured digitized output (i.e. counts, C) to the associated radiometric "brightness" temperature:

$$T = F(C) \tag{1}$$

This function, which is illustrated schematically in Fig. 8 (and where the subscripts c and w refer to the cold and warm calibration points, respectively, and s refers to an Earth scene) depends primarily on channel frequency and instrument temperature, but it could also undergo short term and long term changes due to gain fluctuations and drift due to aging and other effects. Note that others, notably NOAA, use the physical quantity called radiance, which has units of $\text{mW}/\text{m}^2\text{-sr}\text{-cm}^{-1}$, instead of the quantity called brightness temperature that we will use here, which has units of K. It is a simple matter to convert between the two, however.

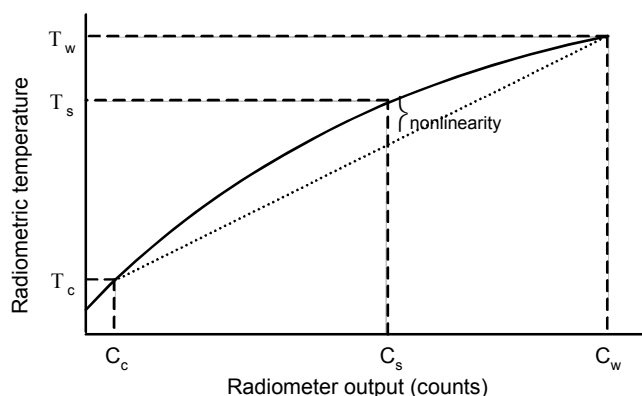


Figure 8. Transfer function schematically

³ "ATMS Radiometric Math Model", NGES Report 12110C (October 2005)

If the transfer function were perfectly linear, then two calibration points would uniquely determine its form at the time of the calibration measurements, since two coefficients could then be computed:

$$F_{\text{lin}}(C) = a_0 + a_1C \quad (2)$$

While it has been a design goal (and a requirement) to make the transfer function as linear as possible, in reality it is slightly nonlinear. To account for the slight nonlinearities we allow for a quadratic term:

$$F_{\text{nonlin}}(C) = a_0 + a_1C + a_2C^2 \quad (3)$$

The magnitude of the quadratic nonlinearity is of course zero at the two calibration points and its functional form can therefore be uniquely expressed as

$$T_{\text{NL}} = 4x(1-x) T_{\text{NL}} \quad (4)$$

where x is a measure of the relative distance of an Earth scene point from the two calibration points,

$$x = (T_s - T_c)/(T_w - T_c) \quad (5)$$

and T_{NL} is the peak nonlinearity, occurring at the midway point, i.e. at $x = 0.5$.

We emphasize that these expressions pertain to a quadratic nonlinearity model – which is thought to be a good approximation, since the nonlinearities are generally quite small. We also note that determining T_{NL} from ground measurements is not straightforward, and detecting changes in its value after launch (a distinct possibility) is even more difficult. In principle, this parameter may be a function of instrument temperature and may have other dependencies as well. The current algorithm allows the choice of using a fixed set of nonlinearity terms or determining those terms as a function of the instrument temperature and the redundancy configuration. The receiver shelf temperature (KKA Shelf, V Shelf, W Shelf, and G Shelf) is used to interpolate between table pairs determined from pre-launch test data. Each table pair consists of a receiver temperature and a nonlinearity term.

For AMSU, the form given in Eq. 3 was used, both by NOAA and by NASA, and the calibration algorithms specified how the coefficients a_0 - a_2 were to be computed. The approach proposed for ATMS is to first use the linear approximation (equivalent to Eq. 2) and then make a quadratic correction per Eq. 4. The linear approximation is simply a representation of a straight line through the two calibration points (the dotted line in Fig. 8):

$$T_{\text{lin}} = T_c + [(T_w - T_c)/(C_w - C_c)] (C - C_c) \quad (6)$$

i.e. the linear coefficients are

$$a_1 = (T_w - T_c)/(C_w - C_c) \quad (7)$$

$$a_0 = T_c - a_1C_c \quad (8)$$

The inverse of a_1 is often called the “gain”, an important measure of radiometer output for a given scene temperature:

$$g = 1/a_1 = (C_w - C_c)/(T_w - T_c) \quad (9)$$

In the following paragraphs we first discuss how the calibration points are obtained. Subsequent sections discuss how the Earth scene brightness temperatures are determined.

5.1 Blackbody view

The internal calibration targets are approximately cylindrical in outline and are made up of pyramid shaped metal structures coated with an absorbing material. Figure 9 shows an AMSU calibration target (the ATMS targets are quite similar). For the larger aperture, the pyramids are about 1 cm across and about 4 cm high. The metal base and core ensures that temperature gradients across the targets are minimal, while the pyramid structure and the absorbing coating ensure that the emissivity is close to 1. The target is surrounded by a metal shroud, which mates very closely with a matching shroud surrounding the rotating reflector antenna, to prevent stray radiation from external sources from affecting the warm calibration measurements. For ATMS, where the antenna moves during calibration measurements, the calibration target is slightly larger than the antenna shroud aperture, so that the antenna has a full view of the target during the entire calibration period.

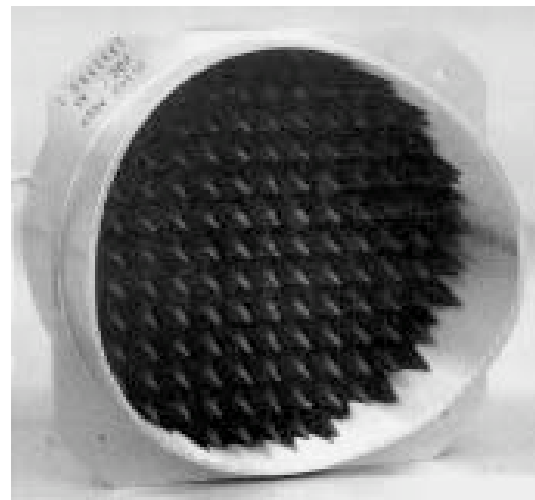


Figure 9. Typical warm load

In order to reduce the effect of random noise, the calibration target is viewed four times consecutively. (Consecutive samplings are used in lieu of a single sampling of longer duration in order to keep the data collection control system simple.) The effective calibration measurement noise, after averaging, is then reduced by a factor of 2 below the NEDT values listed in Table 1. These values can be reduced even further by averaging over several calibration cycles, as we will describe. The four consecutive measurements are assumed to be entirely equivalent, but that assumption remains to be tested, both on the ground and on-orbit. (The calibration algorithms may have to be modified if this assumption turns out to be faulty.)

The emissivity of the calibration targets is required to be at least 0.9999. This is necessary in order to keep radiation that is unavoidably emitted from the radiometer's local oscillators through the antenna and reflected back from the calibration target to a minimum. (Such radiation could masquerade as a radiated brightness temperature of as much as 100 K. An emissivity of 0.9999, and thus a reflectivity of 0.0001, would then yield a reflected contribution of 0.01 K – a negligible amount.) Measured ATMS target emissivities exceed 0.9999, and maximum emission from the antenna has been measured to be less than 100 K (using a “tunable short test”).

The targets are not thermally controlled, but since they are somewhat insulated from external thermal swings (and the entire instrument is thermally insulated from the platform), it is expected that the target temperatures will not change rapidly (less than 0.001 °C/sec) and that temperature gradients across the targets will be minor (less than ± 0.05 °C). To ensure good knowledge of the target temperatures, there are 8 and 7 temperature sensors (Platinum Resistance Thermometers — PRT's) embedded throughout the KAV and WG targets, respectively. Measurement accuracy is better than 0.1 °C. The PRT's are embedded in the metal structure from the back, close to the coated front surface.

One potential problem is that any vertical temperature gradient in the pyramid structure will not be measured and is also difficult to model and predict. There are indications from previous studies that such gradients can have a major effect on calibration accuracy, particularly because they are thought to be frequency dependent (i.e. radiation at the shorter wavelengths may originate from a particular part of the pyramids while longer wavelengths may originate from a different area – e.g., tips vs. troughs). Temperature gradients in a periodic structure as in the ATMS targets can also cause resonant effects such as grating “sidelobes”. The performance on-orbit may therefore be somewhat poorer than as measured on the ground (where benign and controlled conditions are usually maintained). Bias corrections determined from thermal-vacuum tests on the ground may compensate for some of these effects, however.

In general, there will be a small difference between the brightness temperature computed from the physical temperature of the target and its estimated emissivity on one hand and the brightness temperature inferred from the radiometer output on the other. This is caused by effects such as discussed above. One of the objectives of the ground based thermal-vacuum measurements, where operational conditions are simulated as closely as possible, is to determine the magnitude and dependencies of such biases. This is accomplished by observing a NIST-traceable reference target in lieu of an Earth “scene”. Since the brightness temperature of such a target is known with better accuracy than that of the ATMS internal warm loads, it is possible to use it to infer the warm load biases discussed here. Such biases are typically quite small but may be of the same magnitude as the target calibration accuracy and must therefore be accounted for in the calibration processing. The biases, i.e. observed differences between inferred ATMS warm load brightness temperatures and known simulated scene brightness temperatures, may depend on the physical temperature of the receiver system.

5.2 Cold space view

There are 4 cold space calibration beam groups located at 6.66 degrees, 8.33 degrees, 10.00 degrees and 13.33 degrees below the anti-sun normal toward nadir in the scan plane. Which beam group to use is selectable by ground command. Within a beam group, the cosmic background radiation is also sampled four times consecutively, with each sample spaced 1.11 degrees apart. Here, however, the radiative environment is much more complex than for the warm calibration target view. Although the cosmic radiometric temperature is well known (2.726 ± 0.004 K), significant radiation from the earth as well as earth radiation reflected from spacecraft structures can enter the antenna sidelobes. This is illustrated conceptually in Figure 10. As a general rule, we can estimate that on the order of .1-.2 % will be received from the 124° sector that “sees” Earth from an 828 km orbit altitude (828 km for NPOESS, 824 km for NPP). This contribution is then on the order of 1/4-1/2 K, i.e. about $1/10^{\text{th}}$ - $1/5^{\text{th}}$ of the cosmic radiation.

This is not insignificant, but the effect on calibration accuracy is relatively small, as discussed in the next section. Contributions due to reflections from the structures and surfaces on the spacecraft are probably minor. (Radiation emitted from the spacecraft is expected to be negligible, since most surfaces will be covered with MLI blanket – a metallized Mylar material that is highly reflective at microwave frequencies.)

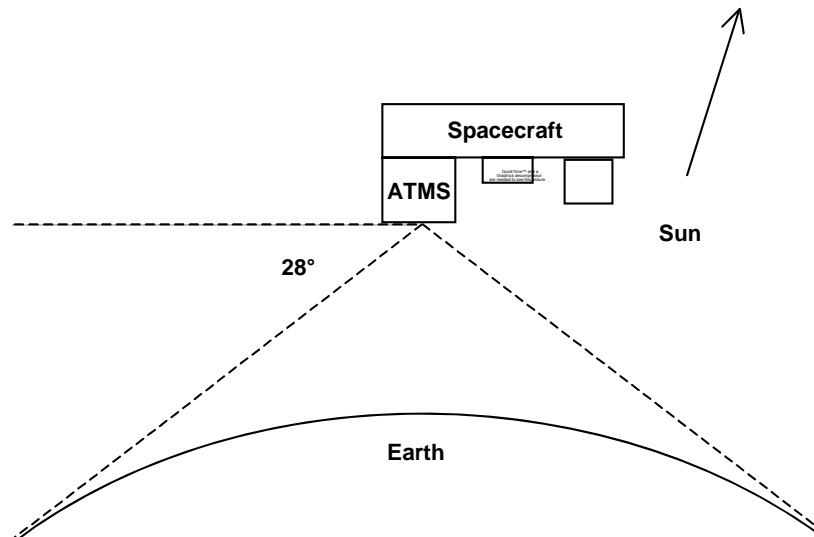


Figure 10. Space view geometry
(flight direction is toward the reader, out of the page)

Figure 10 also suggests that the Earth sidelobe radiation probably depends on the exact pointing direction and is likely to be greatest when the antenna boresight is closest to Earth. This means that, for a given nominal space calibration position, the sidelobe contribution may vary between the four consecutive samples – which cover an angular range in excess of 4°. The baseline algorithm averages these together to reduce the effective noise, but analysis must be undertaken after launch to determine if that is appropriate (just as a similar analysis is required for the warm calibration measurements).

It is common practice to use the Rayleigh-Jeans approximation for brightness temperature, which is essentially that (ignoring the emissivity) the brightness temperature equals the physical temperature,

$$T \approx T \tag{10}$$

This is a low-frequency high-temperature approximation that breaks down for combinations of high frequency and low temperature, which is the case for ATMS in the context of the low brightness temperatures normally encountered during cold calibration. To correct for the resulting error, the cold calibration brightness temperature inputs to the SDR processing algorithm are adjusted (see section 5.3 in the “ATMS Radiometric Math Model” referenced earlier).

Finally, we should note that the cold space view can also be contaminated by the Moon. From time to time (i.e. on a quarterly cycle) the Moon, which is near half-full when seen from the

spacecraft, may approach the field of view of one or more of the space view positions. The worst-case effect, i.e. with the Moon exactly in the boresight direction, is to elevate the space view brightness temperature by up to 20 K for the channels with a 1.1° FOV, up to 5 K for the channels with a 2.2° FOV and 1 K for the channels with a 5.2° FOV. Also in the worst case, the effect may be detectable for a period up to 10 minutes. When this happens, it is necessary to either account for the increase in space view brightness temperature (i.e. model it) or reject the observation from calibration processing based on prediction or detection.

5.3 Sources of errors and uncertainties

In this section we summarize the sources of errors and uncertainties in the calibration process. A detailed analysis can be found in the NGES "Radiometric Math Model" report referenced earlier. Errors can be classified as bias errors, which are uncertainties in the bias corrections applied, and random errors, which are uncertainties due to random fluctuations of the instrument characteristics. We will in general correct for all known biases, so that only their uncertainties remain. We assume that all uncertainties are independent and random and add up in a root-sum-squared (rss) sense. (This is not strictly correct, but the resulting errors in the uncertainty estimates are judged to be relatively small.)

As was explained in the introductory part of this section, the in-flight calibration procedure consists of determining the transfer function at two points — the cold space calibration view and the internal blackbody calibration view — and fixing a quadratic function between these two anchor points, where the amplitude of the quadratic deviation from linearity (denoted by T_{NL} in Eq. 4) is assumed to be fixed for each channel and possibly a function of instrument temperature. The transfer function thus determined is then used to convert earth scene radiometer measurements to a corresponding brightness temperature. The absolute accuracy of this scene brightness temperature is termed the calibration accuracy. (*Calibration accuracy* is strictly defined as the difference between the means of the inferred and the actual brightness temperature when a large blackbody calibration target is placed directly in front of the antenna for an extended period of time.) It can be expressed as

$$\Delta T_b = \text{RSS} \{ x\Delta T_w ; (1-x)\Delta T_c ; 4x(1-x)\Delta T_{NL} ; \Delta T_{\text{sys}} \} \quad (11)$$

where "RSS" means that the result is the square root of the sum of the squares of the terms. The factor x is the relative scene temperature defined in Eq. 5, and ΔT_w , ΔT_c , and ΔT_{NL} are the respective uncertainties in the calibration radiometric temperatures and the nonlinearity amplitude. ΔT_{sys} is an uncertainty due to random instrument fluctuations (e.g., gain fluctuations). Note that no biases are included in Eq. 11; it expresses the uncertainty only.

Although scene temperatures may go as low as 80-90 K at the higher frequencies, the meaningful operational dynamic range is 200-300 K for sounding channels and about 140-300 K for window channels. Substantially lower sounding temperatures are caused by scattering from raindrops or ice above precipitating cells – conditions that currently cause the retrieval process to fail. (It is possible that scattering may be included in the retrieval algorithms in the future, however.) Very transparent window channels, where a low ocean emissivity makes ocean scenes appear radiometrically very cold, are also not crucial to the retrieval processing. Thus, the effective meaningful dynamic range is 200-300 K. With a T_w on the order of 300 K and T_c close to zero, the meaningful dynamic range for x is $2/3-1$. In the worst case ($x \sim 2/3$) the relative weights of the first two terms in Eq. 11 are then $4/9$ and $1/9$, respectively. This means that errors in T_c contribute 4 times less to the overall calibration accuracy than errors in T_w , and for most scenes considerably less than that. It is useful to keep this perspective in mind when the error sources are discussed.

In the following we will briefly discuss the factors contributing to the uncertainties. The interested reader is referred to the Radiometric Math Model document for a thorough and detailed discussion.

Blackbody error sources

These errors stem from *uncertainty* in the knowledge of four factors:

- a) blackbody emissivity
- b) blackbody physical temperature
- c) reflector/shroud coupling losses
- d) reflected local-oscillator leakage

Of these, the second term is expected to dominate.

The *emissivity* is generally known to lie in a range, $[\epsilon_{\min}, 1.0]$, due to limited measurement accuracy. (A typical value for ϵ_{\min} is 0.99993.) This should be interpreted as

$$\epsilon = 1.0 - (1.0 - \epsilon_{\min})/2 \pm \Delta\epsilon \quad (12)$$

where $\Delta\epsilon$ is the estimated uncertainty. It is bounded by $(1.0 - \epsilon_{\min})/2$. (For the example quoted, where ϵ_{\min} is estimated to be 0.99993, the uncertainty would be estimated at < 0.000035 .) An alternative estimate could be based on an analysis of the method used to determine the emissivity (typically by measuring the reflectivity).

The *blackbody physical temperature* is uncertain due to

- a) surface temperature drifts between the time of temperature measurement and the time of radiometer measurement (ΔT_{drift})
- b) temperature gradients in the blackbody (ΔT_{grad})
- c) temperature measurement uncertainties (ΔT_{meas})
- d) vertical gradients and uncertain origin of the radiation (ΔT_{vert})

The last factor is currently unknown, but it is possible it may dominate this term.

The *reflector/shroud coupling losses* occur because the antenna and blackbody shrouds do not mate perfectly, and external radiation (from the interior of the instrument) will enter the antenna through the gap between the shrouds. This effect is uncertain because of uncertainties in measuring and modeling the coupling losses as well as uncertainties in the knowledge of the external radiation. The magnitude of this is expected to be very small and can be ignored.

Finally, the *leakage* signal originating from the local oscillators and emitted by the antenna may be reflected back to the antenna by the blackbody, if its emissivity is not unity (i.e. if its reflectivity is not zero). This is uncertain because the leakage signal is not known precisely and the target reflectivity (or emissivity) is not known precisely. The latter is expected to dominate, and the former can be ignored. (The reflected LO signal may also interfere with itself by changing the operating point of the detector system, which then impacts the intrinsic noise level of the amplifier. Thus, although the LO interference may be well outside the IF passband and therefore not directly measurable, it can still significantly impact the apparent output noise of the system.)

The resulting uncertainty is

$$\Delta T_w = \text{RSS}\{\Delta\epsilon T_w; \Delta T_{\text{drift}}; \Delta T_{\text{grad}}; \Delta T_{\text{meas}}; \Delta T_{\text{vert}}; \Delta\epsilon T_{\text{LO}}\} \quad (13)$$

where T_{LO} is the leakage radiance, expressed as a brightness temperature.

Only the first term is expected to change in orbit, so this can be contracted to

$$\Delta T_w = \{[\Delta \varepsilon T_w]^2 + [\Delta T_{w, \text{fixed}}]^2\}^{1/2} \quad (14)$$

where $\Delta T_{w, \text{fixed}}$ represents the unchanging terms compiled from ground measurements.

Cold calibration (space view) error sources

This error stems from uncertain knowledge of three factors:

- a) Earth contamination through the antenna sidelobes
- b) spacecraft contamination through the antenna sidelobes
- c) the cosmic background temperature

The *sidelobe contamination* is uncertain due to uncertain knowledge of the antenna pattern (i.e. sidelobes) as well as uncertain knowledge of the radiation from Earth and from the spacecraft. (The latter consists mostly of reflected Earth radiation, since most visible surfaces will be covered by reflective materials, as discussed above.) Both effects may be modeled and pre-computed, but the associated uncertainties are expected to be substantial. This is the largest contribution to this term.

We may express the sidelobe radiation as the product of an effective antenna efficiency, a_{eff} , (over the sector that receives this radiation) and an effective scene temperature for that sector, T_{eff} :

$$T_{\text{SL}} = a_{\text{eff}} T_{\text{eff}} \quad (15)$$

The uncertainty is then the sum of two terms,

$$\Delta T_{\text{SL}} = \text{RSS}\{\Delta a_{\text{eff}} T_{\text{eff}} ; a_{\text{eff}} \Delta T_{\text{eff}}\} \quad (16)$$

The uncertainty in a_{eff} is primarily due to uncertain antenna patterns (from which it is usually computed), and the uncertainty in T_{eff} is primarily due to an uncertain or variable mean brightness temperature of the visible Earth disc. There is also an error component caused by representing the sidelobe radiation as the simple product shown in Eq. 15 – in reality this is a double integral, i.e. a convolution between the two. It may be noted that the effective scene temperature varies along the orbit – there are both latitudinal (i.e. intra-orbital), longitudinal (i.e. inter-orbital) and temporal (e.g., inter-seasonal) variations in the effective brightness temperature of the visible portion of the Earth. This may be modeled or estimated in other ways, or it may be ignored and instead carried as an additional uncertainty.

Finally, although the *cosmic background temperature* is well known, there is an uncertainty associated with it. However, it can be ignored here, since the uncertainty of the sidelobe radiation is expected to dominate the cold calibration uncertainty. The result is

$$\Delta T_c \approx \Delta T_{\text{SL}} = \text{RSS}\{\Delta a_{\text{eff}} T_{\text{eff}} ; a_{\text{eff}} \Delta T_{\text{eff}}\} \quad (17)$$

Instrument (transfer function) error sources

This error stems from uncertainty in the knowledge of four factors:

- a) nonlinearities
- b) system noise
- c) system gain drift
- d) bandpass shape changes

The *nonlinearities* can be modeled as a quadratic term that may be a function of a characteristic instrument temperature, as discussed above. This is only an approximation and is therefore uncertain. In addition, as for the blackbody, the instrument temperature is not known precisely. We will, however, ignore the latter effect. The former is expressed in terms of the uncertainty of the peak nonlinearity, ΔT_{NL} in Eq. 11.

The system terms are due to random fluctuations and are characterized in terms of standard deviations. These are channel dependent, as are most of the effects discussed above. The combined effect is expressed as ΔT_{sys} in Eq. 11.

6 Calibration processing steps

In this section we describe how the on-board calibration measurements are used to determine the calibration coefficients, as discussed in Section 5. In summary, the procedure – illustrated in Fig. 11 – is as follows. Each channel is treated separately.

1. Determine the blackbody brightness temperature, T_w , from its physical temperature as measured by the embedded PRT's and a possibly temperature dependent bias correction
2. Estimate the cold-space view brightness temperature, T_c , taking into account earth radiation into the antenna sidelobes and a correction to the Rayleigh-Jeans approximation
3. Average the blackbody and cold-space radiometer counts, C_w and C_c , measured in a calibration cycle (i.e. up to 4 values) and smooth the averages over several calibration cycles
4. Determine the radiometer gain, from Eq. 9
5. Estimate a scene brightness temperature from the linear approximation of Eq. 6
6. Use the linear approximation to estimate the relative brightness temperature, x in Eq. 5
7. Estimate the radiometer nonlinearity amplitude, T_{NL} , in Eq. 4, possibly based on a measured instrument temperature
8. Compute a quadratic correction of the brightness temperature per Eq. 4

This implicit transfer function is applied to the earth-scene radiometer counts for one scan cycle.

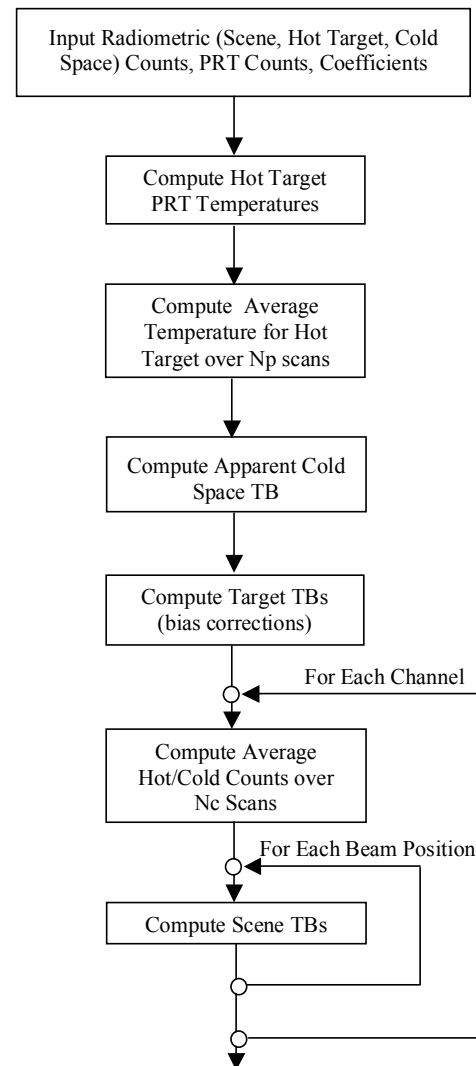


Figure 11. Calibration flow chart

6.1 Physical temperatures

Several calibration steps require the conversion of a PRT raw count to a corresponding physical temperature. The procedure for such conversions is common to all PRTs. In essence, a PRT is a passive sensor with a resistance that is a known function of temperature. An analog-to-digital converter (ADC) outputs a digital ‘count’ that is proportional to the resistance, which is inserted into the telemetry. The conversion to temperature on the ground has two steps. In the first step, the resistance is reconstructed with a linear transfer function that is calibrated with on-board measurements of a known reference resistor (the so-called precision analog monitor – PAM). This conversion is

$$R_{PRT} = R_{PAM} (C_{PRT} - C_{off}) / (C_{PAM} - C_{off}) \quad (18)$$

where C_{off} refers to a reference count with shorted inputs (i.e. zero resistance). (Thus, the essentially linear ADC is “calibrated” on-board with two reference measurements, just as is done for the slightly nonlinear radiometer.)

The second step is to convert the resistance to a temperature value. Here, the transfer function – called the Callendar-Van Dusen equation – is nonlinear:

$$R_x = R_0 \{1 + \alpha[T_x - \delta(T_x/100 - 1)(T_x/100) - \beta(T_x/100 - 1)(T_x/100)^3]\} \quad (19)$$

where the coefficients R_0 , α , β and δ are characteristic (and determined by the manufacturer) for each individual PRT, and the temperature is in °C. This equation is solved for T_x by Newton-Raphson iteration. (A simpler but less robust alternative approach, used with the AMSU systems, is to fit a cubic polynomial, $T = c_0 + c_1C + c_2C^2 + c_3C^3$, to the two functions expressed in Eq. 18 and Eq. 19, which can be done with negligible error.)

Using this method, all PRT readings are converted to temperatures.

6.2 Effective blackbody brightness temperature

Physical temperature

In summary: The warm load physical temperature is determined as the average value derived from the embedded PRT's plus a bias-like correction factor (which is allowed to depend on the receiver's physical temperature). A weighted average in two dimensions (PRT # and across-scan sample) is implemented that allows for a weighted average. This makes it possible to

- a. give more weight to certain PRTs than others
- b. implement a non-equal time-weighted average (i.e. where samples closest in time are given more weight than those more distant)

The weighting coefficients are specified in ancillary processing tables that can be changed at any time.

The result is an effective warm load physical temperature, T_w .

Bias correction

The warm load bias correction may be applied in two ways. The first option applies a fixed bias for each of the 5 bands (K, Ka, V, W and G). The K band covers channel 1. The Ka band covers channel 2. The V band covers channels 3-15. The W band covers channel 16. The G band cover channels 17-22. For the second option, a temperature dependent bias correction is applied for each channel, which is assumed to be of at most quadratic form

$$\Delta T_w = a + bT_{\text{BP}} + cT_{\text{BP}}^2 \quad (20)$$

where the coefficients a , b and c are also specified in the ancillary data tables (one set for each channel) and T_{BP} is an instrument temperature representative of the receiver base plate. This makes it possible to allow for any slightly nonlinear temperature dependent biases that may be determined from ground testing. Extensive analysis of test data is required for this

implementation (e.g., identification of temperature dependence and polynomial functional fits).

Warm load brightness temperature

The warm load brightness temperature is now calculated as

$$T_w = T_w + \Delta T_w \quad (21)$$

6.3 Effective space brightness temperature

Cosmic background temperature

A value of 2.728 K is used for T_c .

Rayleigh-Jeans correction

A correction has been pre-computed that accounts for deviations from the Rayleigh-Jeans approximation at the low space brightness temperatures.

Sidelobe bias correction

As discussed above, there may be substantial radiation received from the relatively warm Earth through the antenna sidelobes while the antenna is pointing at space. A set of correction values (one for each channel) has been computed from the measured antenna patterns and a simple climatological model of the Earth. (This does not account for the fact that the actual mean scene temperature varies, as we discussed above.) The current implementation allows 2 choices, either using one value for each of the 5 bands (K, Ka, V, W and G) or one value for each of the 22 channels.

Space view brightness temperature

The cold calibration brightness temperature is now calculated as

$$T_c = (2.726 + \Delta T_{RJ}) + \Delta T_{SL} \quad (22)$$

where the values within the parentheses are pre-computed, stored in ancillary tables and simply read from those tables.

Lunar contamination

As we discussed above, it is likely that the Moon will enter the cold-calibration FOV from time to time and contaminate the apparent space brightness temperature. The cold space view temperature increase caused by the lunar contamination is estimated⁴ as:

$$\Delta T_c = \exp\left[-\frac{(\alpha - \alpha_0)^2}{2\alpha_s^2}\right] \exp\left[-\frac{(\delta - \delta_0)^2}{2\delta_s^2}\right] \times \beta \times T_{moon} \times \left(\frac{60.3 \times 6278}{d}\right)^2 \quad (23)$$

Where α : lunar azimuth [degrees]
 α_0 : FOV center azimuth [degrees]
 α_s : FOV azimuth size factor [degrees]
 δ : lunar elevation [degrees]

⁴ Seiichiro Kigawa and Tsan Mo: "An Algorithm for Correction of Lunar Contamination in AMSU-A Data", NOAA Technical Report NESDIS 111 (Dec 2002)

- δ_0 : FOV center elevation [degrees]
- δ_s : FOV elevation size factor [degrees]
- β : nominal area ration of moon to FOV
- d : distance between satellite and moon [km]
- T_{moon} : effective moon temperature [K]
 $= 95.21 + 104.63(1 - \cos \theta) + 11.62(1 + \cos 2\theta)$
- θ : separation angle between moon and sun ($\theta=180^\circ$ in case of Full Moon)

Eq (23) may be simplified if the following approximations are made:

- (a) assuming that the antenna patterns are circularly symmetric,
- (b) ignoring the FOV center offsets, and
- (c) ignoring the satellite to moon distance variation correction.

Equation (23) is then reduced to:

$$\Delta T_c = \exp\left[-\frac{\gamma^2}{2\gamma_s^2}\right] \times \beta \times T_{\text{moon}} \quad (24)$$

Where γ : angle between the cold space view and the moon [degrees]

$$\gamma_s = \frac{\gamma_{3dB}}{2.35} \quad \text{where } \gamma_{3dB} \text{ is the 3dB beamwidth [degrees]}$$

$$\beta = \frac{1}{2} \left(\frac{r_{\text{moon}}}{\gamma_s} \right)^2 \quad \text{where radius of the moon: } r_{\text{moon}} = 0.255 \text{ deg}$$

If ΔT_c is larger than a threshold, the cold space view is not included in the calibration. ΔT_c is used for excluding contaminated samples, but is otherwise not used to correct the cold space temperature.

6.4 Radiometric calibration counts

Each of the two calibration targets (i.e. the warm load and cold space) is sampled four times in succession. The results are digital "counts" which represent the radiometer's output. It is assumed that the radiative environment does not change between successive samplings, so that any differences between the measurements are strictly due to noise — which can be reduced by averaging or smoothing the measurements. However, as discussed above, this assumption must be tested on-orbit and may not be valid. Should that be the case, the present calibration algorithms need to be modified somewhat.

The procedure implemented is simply to compute a count averaged over the four in-scan samples and over several scans. Ancillary tables are used to specify the respective weights. This approach essentially puts the main burden on the analysis of ground test data and the derivation of the proper coefficients from that data. Here, we will only point out that caution must be exercised to ensure that the averaging interval in the time domain is commensurate with the measured 1/f-noise behavior. Typically, a power spectrum is obtained and analyzed to determine where the 1/f "knee" is located. This then dictates the maximum length of the averaging interval. (In the case

of PRT readings and derived physical target brightness temperatures, this is not a concern, and the averaging or fitting interval can be much greater for those quantities than for the radiometer counts.)

6.5 Earth scene brightness temperatures

First the gain g is computed per Eq. 9. This allows a linear estimate of the brightness temperature, T_{lin} to be determined, which in turn enables the computation of a corresponding x -factor per Eq. 5. Finally, Eq. 4 is used to compute a nonlinear correction term. The sequence is listed below:

$$g = (C_w - C_c)/(T_w - T_c) \quad (25)$$

$$T_{lin} = T_w + (C - C_w)/g \quad (26)$$

$$x_{lin} = (T_{lin} - T_c)/(T_w - T_c) \quad (27)$$

$$T_{NL} = 4x_{lin}(1-x_{lin}) T_{NL} \quad (28)$$

$$T = T_{lin} + T_{NL} \quad (29)$$

This is done for each channel and for each scan position.

6.6 Data quality control

The SDR code examined for the first version of this document contains only rudimentary data quality control (QC) and quality assessment (QA). Subsequent algorithm updates have incorporated additional quality checking process.

PRT Quality Checks:

1) PRT quality check – limits

The converted warm load PRT temperatures are checked against predetermined gross limits. Those which fall outside the limits are considered “bad”:

$$T_i < T_{low} \text{ or } T_i > T_{upp} \rightarrow \text{“bad-}T_i\text{”}$$

2) PRT quality check – self consistency

The PRT temperatures are next checked for internal consistency. This is done by comparing all temperatures not flagged as bad with each other. Any PRT’s temperature that differs by more than a fixed limit from at least two other PRTs readings will be flagged as “bad”:

$$|T_i - T_j| > \Delta T_{max} \text{ and } |T_i - T_n| > \Delta T_{max} \rightarrow \text{“bad-}T_i\text{”}$$

The number of “good” PRTs is then checked. If there are less than 5 “good” PRTs for the KAV target or 4 for the WG target, all PRTs within that group will be flagged as “bad”. These numbers can be adjusted in the ancillary parameter file. “Bad” PRTs are excluded from the calibration process.

3) PRT quality check – data sufficiency

If the weight-sum of “good” PRT readings used in the multi-scans averaging falls below a specified percentage, it is deemed not possible to reliably determine the warm load temperature for the current calibration cycle:

$$(\sum_i W_i)/W_{\text{total}} < W_{\text{threshold_prt}} \rightarrow \text{“bad-}\bar{T}_w\text{”}$$

Failing the data sufficiency test will result in an unsuccessful calibration cycle.

Warm Count Quality Checks:

1) Quality check – limits

Each count from each channel is checked against pre-defined channel-specific gross limits. Those which fall outside the limits are flagged as “bad”:

$$Cw_i < Cw_{\text{low}} \text{ or } Cw_i > Cw_{\text{upp}} \rightarrow \text{“bad-}Cw_i\text{”}$$

2) Quality check – self consistency

The counts are next checked for internal consistency. This is done by checking each count not flagged as “bad” against other counts in the same scan. Any count that differs by more than a fixed limit from at least two other counts will be flagged as “bad”:

$$|Cw_i - Cw_j| > \Delta Cw_{\text{max}} \text{ and } |Cw_i - Cw_k| > \Delta Cw_{\text{max}} \rightarrow \text{“bad-}Cw_i\text{”}$$

The number of “good” samples is then checked. If there are less than 3 “good” samples, this scan will be flagged as “bad” and not included in the multi-scans averaging.

3) Quality check – gain error

If the lowest “good” warm count is smaller than or equal to the highest “good” cold count, all the warm counts and cold counts with this scan will be flagged as “bad” and not included in the multi-scans averaging.

4) Quality check – data sufficiency

If the weight-sum of all “good” scans falls below a specified percentage, it is deemed not possible to reliably determine the averaged warm count for the current calibration cycle. Failing the data sufficiency test will result in an unsuccessful calibration cycle.

Cold Count Quality Checks:

The cold count quality checks are identical to the warm count checks, with limits appropriate for the cold counts.

All the limits and thresholds would be set initially pre-launch to allow all data to pass through. After some operational experience has been gained after launch, these numbers shall be adjusted accordingly.

7 Scan Bias Correction

The observations are subject to scan bias that needs to be corrected for before the brightness temperatures can be used in any meaningful way. This is not a calibration issue, but it should be dealt with in the SDR processing. The output of the calibration processing is defined as the “antenna temperature”, which is then corrected for the scan bias to give the “brightness temperature”. The current implementation uses the form

$$T_b = c_0 + c_1 T_a \quad (30)$$

T_a is the calibrated “antenna temperature”. c_0 and c_1 are correction coefficients for each channel and each scan position. Analysis of the post-launch Cal/Val data is required for deriving these coefficients.